InSAR Simulation and Speeded-Up Robust Features Algorithm for Terrain Relative Navigation in PSRs on the Moon

Niutao Liu, *Member, IEEE*, and Ya-Qiu Jin, *Life Fellow, IEEE*

***Abstract*—Landing in the permanently shadowed regions (PSRs) on the Moon requires high-resolution topographic information and accurate navigation. Owing to low Sun elevation angles, there is no direct solar illumination in PSR, making it difficult to acquire high-resolution optical images for terrain relative navigation (TRN). Synthetic aperture radar (SAR) onboard lunar orbiter can acquire the high-resolution digital elevation model (DEM) of PSR with the interference phases from repeat-passes, or alternatively, from multiantenna observations in a single orbit pass. In this article, SAR images from dual-antenna observations obtained in single orbit passes are simulated with two-scale model and Range-Doppler algorithm for the interference phases based on the DEM data from the lunar orbiter laser altimeter (LOLA). Hence, we generate DEMs of PSR in two prominent lunar south polar craters, Shoemaker and Shackleton. After geometric correction, the influence of radar parallax in DEM data are removed. The generated DEM data are used to illustrate the possibility of TRN in PSR with the image-matching algorithm. The slope angle image of the PSR from the generated DEM is taken as the reference image for navigation, while high-resolution slope angle image from LOLA DEM data is taken as the real-time image from the flyer. The speeded-up robust features algorithm matches the feature points in the reference image and real-time image. The location of the matched points determines the position and motion vector of the flyer. The simulation proves the DEM data from InSAR can provide detailed topographic information and can be used for navigation in regions of permanent shadows.**

***Index Terms*—Digital elevation model (DEM), interferometric synthetic aperture radar (InSAR), Moon, navigation, permanently shadowed region (PSR), scattering.**

I. Introduction

THE extremely low temperatures in permanently shadowed regions (PSRs) on the Moon make it possible to preserve water ice for long time [1]. Many countries have proposed missions to explore and map the extent of the PSRs [2], [3]. In China's Chang'e 7 mission, a mini-flyer will fly into PSR for in-suit detection and measurement of abundances of water ice [2].

Manuscript received 13 July 2023; revised 28 September 2023 and 9 November 2023; accepted 30 November 2023. Date of publication 5 December 2023; date of current version 14 December 2023. This work was supported in part by the National Natural Science Foundation of China under Grant 62201154. *(Corresponding author: Niutao Liu.)*

The authors are with the Key Laboratory of Information Science of Electromagnetic Waves (MoE), Fudan University, Shanghai 200433, China (e-mail: ntliu@fudan.edu.cn; yqjin@fudan.edu.cn).

Digital Object Identifier 10.1109/JSTARS.2023.3339237

The flyer, which is powered by the unsymmetrical dimethylhydrazine-fueled engine, will be released from the top of the lander. The flying distance can reach 30 km in a round trip [4]. Rocks and small craters in PSR will endanger the safety of the flyer when landing. The spatial extent of the flat and smooth regions suitable for landing in the PSR are usually less than several hundred meters [5]. Accurate positioning is necessary to ensure a successful landing on the small flat regions. High-resolution topographic information is critical for terrain relative navigation (TRN) in PSR. When landing at solar illuminated regions, high-resolution optical images can be used for TRN and hazard avoidance. However, high-resolution optical images are unavailable in PSR.

A digital elevation model (DEM) acquired by the lunar orbiter laser altimeter (LOLA) onboard lunar reconnaissance orbiter (LRO) is available for TRN [6], [7]. The resolution of the DEM data increases with the latitude. Owing to LRO's polar orbit and converging ground tracks, the effective resolution of the LOLA DEM reaches 5 m/pixel in the high polar areas. However, the lunar polar DEMs with 5-m resolution suffer the geometric errors caused by the attitude uncertainty [7].

By matching the DEM data obtained by the laser imaging sensor on the flyer and the DEM data from the laser altimeter [8], the real-time position and motion vector of the flyer can be determined; but as the lander descends to low altitudes and approaches the surface, DEMs of high spatial resolution are required. The resolution of the DEM from the laser altimeter onboard lunar orbiter may be not sufficient to distinguish the terrain features of the observed small area [7]. Real-time positioning at low altitude and during descending period requires high-resolution DEM data.

Synthetic aperture radar (SAR) can acquire the detailed topography information by transmitting and receiving the scattered electromagnetic waves. The scattering coefficients and its products can be used to analyze the physical properties of the terrain [9], [10], [11], [12]. The Mini-RF onboard LRO and dual-frequency onboard Chandrayaan-2 have obtained compact polarization and fully pol SAR images [9], [10]. China's Chang'e 7 satellite plans to carry a dual-frequency SAR, whose resolution can reach 0.3 m, working at L band and Ku band for PSR detection [13]. With the repeat-pass or dual-antenna observations of a same region, interference phases from the SAR images can produce the DEM data of the lunar surface, whose performance will allow for topographic mapping in PSRs at high

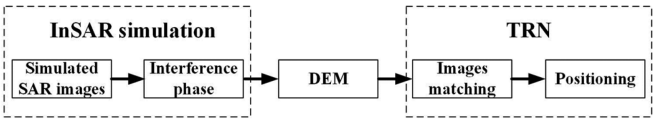

Fig. 1. Basic work concept.

resolution. The resolution of the generated DEM data may reach several meters. The generated DEM data can be used for TRN with the image-matching algorithm.

Area-based and feature-based image registration methods have been widely used. Area-based registration, such as matching with the correlation coefficient, is one possible method for TRN [6]. However, this method is not applicable when the resolutions or the rotation angles of images are different. Feature-based methods, such as SIFT [14], are applicable even though the resolution and rotation angles have changed. Based on SIFT, a speeded-up robust features (SURF) algorithm is proposed [15]. With the combination of integral image and Harris feature, the speed of the algorithm is greatly improved.

In this article, the interferometric SAR (InSAR) images under dual antenna observations are simulated for the interference phases, which can produce the DEM data for TRN. The lunar topography is constructed by the DEM data of the PSRs in crater Shoemaker and Shackleton, which are potential deposits of water ice near the south pole, from the LOLA onboard LRO to model the backscattered echoes with the two-scale rough surface model. The Range-Doppler algorithm (RDA) produce the SAR images with the simulated radar echoes in time domain when chirp pulses are transmitted. Then, the interference phases from the simulation produce the DEM data after removing the phases of flat ground. The geometric deformation in SAR images caused by undulating topography is corrected with the generated DEM data. The slope angle image derived from the generated DEM data is taken as reference image and the slope angle image from the LOLA DEM data is taken as the real-time image from the flyer. The SURF algorithm matches the feature points in two images to estimate the position and motion vector of the flyer. The basic work concept is shown in Fig. 1.

The article is organized as follows. Section II introduces the simulation of dual-antenna SAR images. Section III presents the generation of DEM with interference phases. In Section IV, SURF algorithm is introduced for image matching and TRN with DEM from InSAR. Section V discusses the range of radar incidence angle to avoid layover and shadow effect. Finally, Section VI concludes this article.

II. SAR Image Simulation

A. Scattering Models

The DEM data from LOLA onboard LRO are divided into small triangle meshes to construct the lunar topography. Neighboring points of the DEM data constitute the vertexes of the divided triangle meshes [16]. The component S_{pq}^n of the scattering matrix of the mesh n is [17]

$$S_{pq}^n = \gamma_{pq}^n \sqrt{\frac{A_n}{4\pi}} \tag{1}$$

S_{pq}^n depends on the area A_n and the reflectivity γ_{pq}^n of the mesh n. The subscripts present the polarization. q means the transmitted polarization and p is the received polarization [18].

The scattering matrix $\bar{\bar{\gamma}}$ in the principal reference system is [16]

$$\bar{\bar{\gamma}} = \bar{\bar{U}}^{-1}(\Delta) \cdot \bar{\bar{\gamma}}' \cdot \bar{\bar{U}}(\Delta). \tag{2}$$

where Δ is the rotation angle of the pol-base. The rotation matrix $\bar{\bar{U}}(\Delta)$ is [16]

$$\bar{\bar{U}}(\Delta) = \begin{bmatrix} \cos\Delta & \sin\Delta \\ -\sin\Delta & \cos\Delta \end{bmatrix}. \tag{3}$$

$\bar{\bar{\gamma}}'$ is the scattering matrix in the local coordinate system. $\bar{\bar{\gamma}}'$ can be written as [19]

$$\bar{\bar{\gamma}}' = \begin{bmatrix} a_{\mathrm{HH}} & 0 \\ 0 & a_{\mathrm{VV}} \end{bmatrix} \cdot w(\theta). \tag{4}$$

At small local incidence angle, quasi-specular scatterings dominate. The Kirchhoff approximation (KA) can describe the scatterings from meshes and there is [20], [21]

$$a_{\mathrm{HH}} = \frac{1-\sqrt{\varepsilon_r}}{1+\sqrt{\varepsilon_r}}. \tag{5}$$

$$a_{\mathrm{VV}} = \frac{1-\sqrt{\varepsilon_r}}{1+\sqrt{\varepsilon_r}}. \tag{6}$$

$$\left\langle |w(\theta)|^2 \right\rangle = \frac{1}{4\cos^4\theta\delta_1^2/L_1^2} \exp\left[-\frac{\tan^2\theta}{4\delta_1^2/L_1^2}\right]. \tag{7}$$

At large incidence angle, small-perturbation method is adopted to simulate the scatterings from each mesh [20], [21]

$$a_{\mathrm{HH}} = \frac{\cos\theta - \sqrt{\varepsilon_r - \sin^2\theta}}{\cos\theta + \sqrt{\varepsilon_r - \sin^2\theta}} \tag{8}$$

$$a_{\mathrm{VV}} = (\varepsilon_r - 1)\frac{\sin^2\theta - \varepsilon_r(1+\sin^2\theta)}{\left[\varepsilon_r\cos\theta + (\varepsilon_r - \sin^2\theta)^{1/2}\right]^2} \tag{9}$$

$$\left\langle |w(\theta)|^2 \right\rangle = 4k^4\delta_2^2\cos^4\theta L_2^2 \exp\left[-(kL_2\sin\theta)^2\right]. \tag{10}$$

Here, the real and imagery parts of the complex variable $w(\theta)$ are two independent Gaussian random variables with zero-mean [19]. In the simulation, it is assumed that the root mean square slope of KA is $\sqrt{2}\delta_1/L_1 = 0.08$. For SPM, the correlated length is $L_2 = 3/k$ and the surface standard deviation is $\delta_2 = 0.3/k$ [18]. The relative dielectric constant of regolith is assumed to be 4, which is in the range of the measurement [22]. When $\langle|\gamma'_{pq}|^2\rangle$ of KA is large at small incidence angles, KA is utilized to simulate $\bar{\bar{\gamma}}'$. Otherwise, SPM is used [18].

B. SAR Imaging Algorithm

SAR system transmits chirp modulation pulses and receives raw signals in time domain, which consists of the scatterings

from each mesh in the illuminated region and can be written as [23]

$$h_{pq}(t,T) = \sum S_{pq}^{n} s^{n}(t,T) \tag{11}$$

where [24]

$$s^{n}(t,T) = \prod\left[\frac{t-2R^{n}/c}{\tau/2}\right]\prod\left[\frac{vT-x^{n}}{L_s/2}\right] \times \exp\left\{-i4\pi\frac{R^{n}}{\lambda}+i\pi K_r\left(t-\frac{2R^{n}}{c}\right)^{2}\right\} \tag{12}$$

$$\prod(t) = \begin{cases} 1 & |t| \le 1 \\ 0 & |t| > 1 \end{cases}. \tag{13}$$

The variables are defined as follows.

1) τ is the pulsewidth.
2) t is the time.
3) vT is the azimuth coordinate of the antenna position. T is the azimuth time. v is the velocity of the satellite.
4) x^n is the azimuth coordinate of the mesh n.
5) R^n is the distance between the antenna and the mesh n.
6) c is the speed of light in vacuum.
7) $L_s = \lambda R/L_A$ is the real antenna azimuth footprint.L_A is the azimuthal dimension of the real antenna. λ is the wavelength.
8) $K_r = B/\tau$ is the chirp rate. B is the bandwidth.

In the simulation, the parameter of Chandrayaan-2 and DFSAR are utilized. The altitude of Chandrayaan-2 spacecraft is about 100 km [10]. The incidence angles of the DFSAR is 26° at the center of the SAR image. The incidence angles vary slightly with range distance. The central frequency is 1.25 GHz. The speed of the Chandrayaan-2 spacecraft is about 1.6 km/s. The resolution in ground range direction is [18]

$$r_g = \frac{c}{2B\sin\theta_0} \tag{14}$$

where θ_0 is the incidence angle. The resolution in azimuth is

$$r_a = L_A/2. \tag{15}$$

The resolutions in ground range and azimuth are both set at 10 m/pixel in simulations. The sampling rate is set at $2B$ and the spatial resolution in ground range is $r_g/2$. The pulse repetition frequency is 2 times of the Doppler bandwidth. The spatial resolution in azimuth is $r_a/2$.

Range compression is performed on the signal in frequency domain in range, which is derived with FFT in range direction. After applying IFFT on the signal in range, FFT is applied on the signal in azimuth. Then, the RDA and azimuth compression are performed before applying IFFT in azimuth to obtain the polarized scattering components I_{pq}. In SAR imaging, the sidelobes will influence the correlation coefficients between two SAR images. The strong backscattering from the crater wall facing the radar will reduce the correlation coefficients at the crater wall facing away from the radar because of the sidelobes. Here, Hamming window is used to suppress sidelobes. The number of the meshes in a resolution should be more than 4 [19]. The backscattering coefficient is

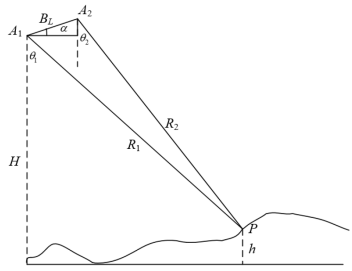

Fig. 2. View geometry of antennas.

$$\sigma_{pq}^{0} = \frac{4\pi|I_{pq}|^{2}}{A_0} \tag{16}$$

where A_0 is the area of each resolution.

III. DEM From InSAR

A. Method

It is assumed that two antennas are carried by a satellite, as shown in Fig. 2. The length of the selected area is much less than the radius of the Moon (1737.4 km). Considering that we work on local areas, we ignore the curvature of the lunar sphere. The distance between antenna A_1 and A_2 is $B_{\rm L}$. The incidence angle of antenna A_1 is θ_1 and the incidence angle of antenna A2 is θ_2. The distance between the antenna A_1 and the point P is R_1 and the distance between the antenna A_2 and the point P is R_2. H is the altitude of the satellite. In the simulation, it is assumed that $B_{\rm L} = 8$ m and $\alpha = 30°$. The interference phase between the observations from two antennas at point P is $\Delta\phi_0$. The interference phase $\Delta\phi_0$, which includes the flat-Earth phase, changes with the distance in ground range direction. The flat-Earth phase can be removed according to the distance between each pixel and the antennas. The interference phase without flat-Earth phase can be written as $\Delta\phi$. The altitude h at the point P can be derived with the interference phase as [25], [26], [27]

$$h = -\frac{\Delta\phi\lambda R_1\sin\theta_1}{4\pi B_L\cos(\theta_1-\alpha)} \tag{17}$$

where λ is the wavelength.

B. Generation of DEM

The interiors of craters Shoemaker and Shackleton are two potential repositories of water ice [28]. The slope angle near the lunar south pole is shown in Fig. 3. We selected two regions of 4 km × 4 km within the two craters, which are included in the white boxes in Fig. 3.

The LOLA DEM data of the selected PSR in crater Shoemaker at 88.1°S, 40.2°E are shown in Fig. 4(a). The resolution of the DEM from LOLA is 10 m/pixel [7]. The slope angles are shown in Fig. 4(b). Linear interpretation is applied to generate DEM data in SAR simulation with resolution of 5 m/pixel. The resolution of the divided meshes are 5 m/pixel. The spatial resolutions of the simulated SAR images are both 5 m/pixel in

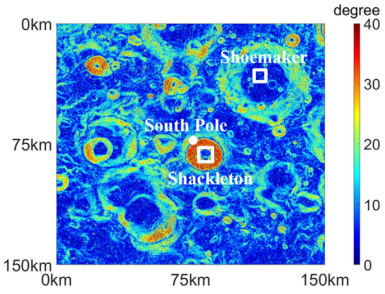

Fig. 3. LOLA slope angles of crater Shoemaker and Shackleton.

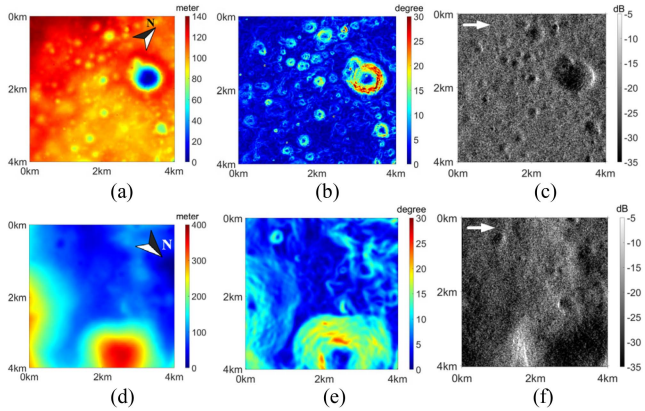

Fig. 4. LOLA DEM data and the simulated SAR image of PSR in crater Shoemaker: (a) DEM data with resolution of 10 m/pixel; (b) slope angles; and (c) simulated σ^0_{HH}. LOLA DEM data and the simulated SAR image of PSR in crater Shackleton: (d) DEM data with resolution of 10 m/pixel; (e) slope angles; and (f) simulated σ^0_{HH}. The white arrow indicates the observation direction.

azimuth and ground range directions, which are equal to $r_a/2$ and $r_g/2$, respectively. The simulated σ^0_{HH} is shown in Fig. 4(c). The satellite observes the PSR from the left. The crater walls facing the radar have strong backscattering because of small local incidence angles. Fig. 4(d)–(f) presents the LOLA DEM data, the slope angle image, and simulated σ^0_{HH} of the PSR in crater Shackleton at 89.7°S, 130.0°E.

With the simulated SAR images from two antennas, the interference phase $\Delta\phi_0$ of PSR in crater Shoemaker can be calculated, as shown in Fig. 5(a). In the simulated SAR images, the azimuth positions of observation are the same. Registration of SAR images in range direction is performed before calculating $\Delta\phi_0$. After removing the flat-Earth phase, the interference phase $\Delta\phi$ of crater Shoemaker is shown in Fig. 5(b). Fig. 5(c) and (d) presents the $\Delta\phi_0$ and $\Delta\phi$ of PSR in crater Shackleton. The selected PSR locates at the flat bottom of the crater Shoemaker. According to (17), the variance of 2π in $\Delta\phi$ results from a change of about 700 m in altitude. Such large change in altitude mainly locates at the crater wall of large craters. The variances in altitude of lunar surface are smaller than 700 m in Fig. 4(a) and (c). As a result, the changes in $\Delta\phi$ in Fig. 5(b) and (d) are in the range of $-\pi$ to π. Phase unwrapping is not performed.

With (17), the DEM data can be derived from the interference phases. An 8×8 sliding window with a moving gap of 4 pixel is utilized to reduce the fluctuation in the generated DEM caused

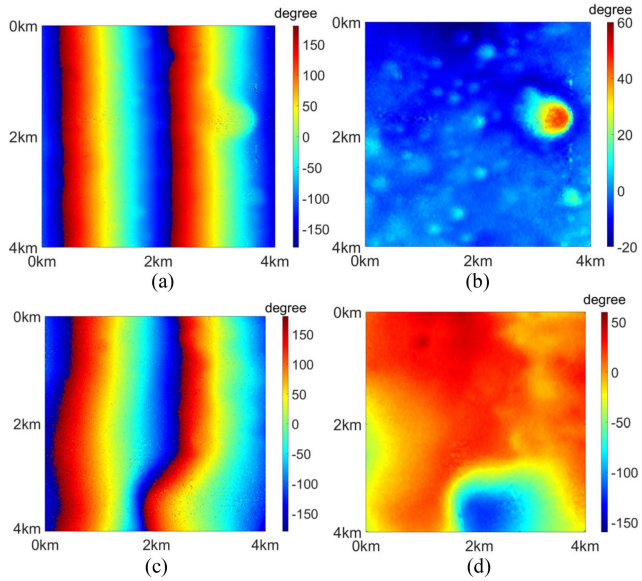

Fig. 5. Interference phases of PSR in crater Shoemaker: (a) $\Delta\phi_0$ with flat-Earth phase and (b) $\Delta\phi$ without flat-Earth phase. The interference phases of PSR in crater Shackleton: (c) $\Delta\phi_0$ with flat-Earth phase and (d) $\Delta\phi$ without flat-Earth phase.

by the noise. The spatial resolution of the generated DEM data is 20 m/pixel. The position of a target in SAR image depends on the distance from the antenna. The variance in altitude will result in radar parallax in range direction. The width of the crater wall facing away from the radar will be extended and the width of the crater wall facing the radar will be reduced. As a result, radar parallax makes the slopes facing the radar increase and the slopes facing away from the radar decrease. With the generated DEM data, the distance between each mesh and the antenna can be calculated. Interpretation method is utilized to remove the influence of radar parallax in DEM data (geometric correction) [29]. Fig. 6(a) and (b) presents the generated DEM data and slope angles of crater Shoemaker after correction. Fig. 6(c) and (d) shows the generated DEM data and slope angles of crater Shackleton. The slope angles from the generated DEM data are then used in TRN.

IV. TRN IN PSR

A. SURF Algorithm

To detect feature points, the SURF algorithm utilizes the approximated determinant of the Hessian matrix [14]. It derives the components of the Hessian matrix by convolving the image with the Gaussian second-order derivative, while approximating Gaussian filters with box filters. The algorithm calculates the determinants of the Hessian matrix using filters of different sizes, and sets a threshold to select feature points based on their determinants [6].

The descriptors of each feature points are constructed for matching [15]. To ensure the descriptors are rotation invariant, the algorithm determines the dominant orientation of each feature point. This is done by calculating the Haar wavelet responses

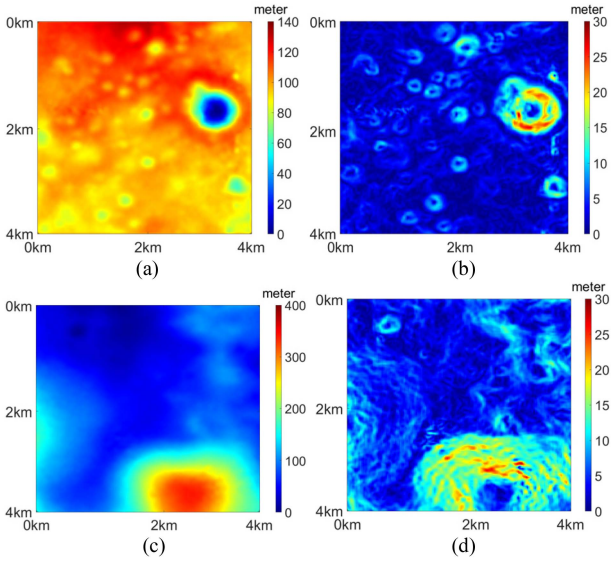

Fig. 6. Generated DEM and slope angles of PSR in crater Shoemaker with a resolution of 20 m/pixel: (a) DEM and (b) slope angles. The generated DEM and slope angles of PSR in crater Shackleton with a resolution of 20 m/pixel: (c) DEM and (d) slope angles.

in the horizontal and vertical directions within a circular neighborhood around the interest point. The size of the neighborhood and wavelets depend on the scale of the detected interest point. Using the calculated vertical and horizontal responses, the algorithm determines the dominant orientation.

Then, a square area around the feature point oriented along the dominant orientation are selected [15]. The square area is divided into 4×4 small subregions and Haar wavelet response of each subregion are calculated. The size of the Haar wavelet and the square area depend on the scale of the feature point. The descriptor of each subregion, with size of $4 \times 4 \times 4$, are calculated by summing up the wavelet responses.

The algorithm uses the method of exhaustion to search for matched points with the sum of squared difference (SSD). It calculates the SSDs between all feature points in two images. A threshold is used to select the potential matched feature points. The picked pairs of feature points may still contain the mismatched points.

The M-estimate sample consensus (MSAC) method is applied to reject the mismatched points [30]. The method picks three pairs of feature points randomly to calculate the affine transformation matrix between two images. The transformation parameters can be derived with the coordinates of the matched points. If the transformation error of two matched points is larger than the threshold, this pair is rejected. Repeating the aforementioned steps until the cost function reaches the minimum. At last, the mismatched points will be rejected according to the transformation geometry.

Using the coordinates of the matched pairs in real-time and reference images, the geometry transformation matrix would be estimated with the least-square method [6] as follows:

$$\begin{bmatrix} X \\ Y \end{bmatrix} = \begin{bmatrix} m_1 & n_1 \\ m_2 & n_2 \end{bmatrix} \begin{bmatrix} x \\ y \end{bmatrix} + \begin{bmatrix} p_1 \\ p_2 \end{bmatrix} \tag{18}$$

where (x, y) are the coordinates of the matched points in the real-time image and (X, Y) are the coordinates of the matched points in the reference image. The real-time position of the flyer in the reference image, which is geocoded, can be obtained with the geometry transformation matrix. The transformation parameters m_1, n_1, p_1, m_2, n_2, and p_2 can be estimated with the coordinates of three pairs of feature points. The rotation angle φ and scaling factor s between two images are able to be inversed with the transformation matrix [6]

$$\begin{bmatrix} m_1 & n_1 \\ m_2 & n_2 \end{bmatrix} = \begin{bmatrix} \cos\varphi & -\sin\varphi \\ \sin\varphi & \cos\varphi \end{bmatrix} \begin{bmatrix} s & 0 \\ 0 & s \end{bmatrix}. \tag{19}$$

With the rotation angle φ, the flying direction can be estimated.

B. TRN in PSR

Fig. 7(a) presents the matched images of PSR in crater Shoemaker with SURF. The resolution of the real-time image is 10 m/pixel and the resolution of the reference image from InSAR is 20 m/pixel. There is no rotation angle in the real-time image. In total, 27 pairs of matched points are extracted with SURF. The estimated rotation angle of the real-time image from the reference image is 0.30°. The estimated scaling factor of the resolutions between two images is 0.50. The maximum registration error is 1.2 pixel and the average registration error is 0.5 pixel.

In Fig. 7(b), the real-time image is rotated by 45°. There are 23 pairs of matched points. The estimated rotation angle is 44.95° and the scaling factor is 0.50. The maximum registration error is 1.4 pixel, and the average registration error is 0.5 pixel.

Fig. 7(c) presents the matched images of PSR in crater Shackleton with SURF algorithm. The rotation angle of the real-time image is 0°. In total, 17 pairs of feature points are matched with the algorithm. The estimated rotation angle of the real-time image from the reference image is 0.09° and the estimated scaling factor of the resolutions is 0.50. The maximum registration error is 1.3 pixel, while the average registration error is 0.7 pixel.

In Fig. 7(d), the real-time image in crater Shackleton is rotated by 60° from the reference image. There are 23 pairs of matched points. The estimated rotation angle is 61.5° and the scaling factor is 0.51. The maximum registration error is 0.9 pixel and the average registration error is 0.5 pixel. Overall, the error in the estimated flying direction is less than 1.5° and the maximum error in position is less than 1.5 pixel. The result indicates the robustness of the SURF algorithm under different scales and rotation angles.

V. Discussion

In Fig. 8, if the slope angle of the crater wall DE, which is facing away from the radar, is larger than the residual angle of the incidence angle, the slope DE will be shaded and no information of the shaded crater can be obtained. For crater walls CD facing the radar, if the slope angle of the crater wall is larger than the incidence angle, scatterings from the slope CD in Fig. 8 will lay

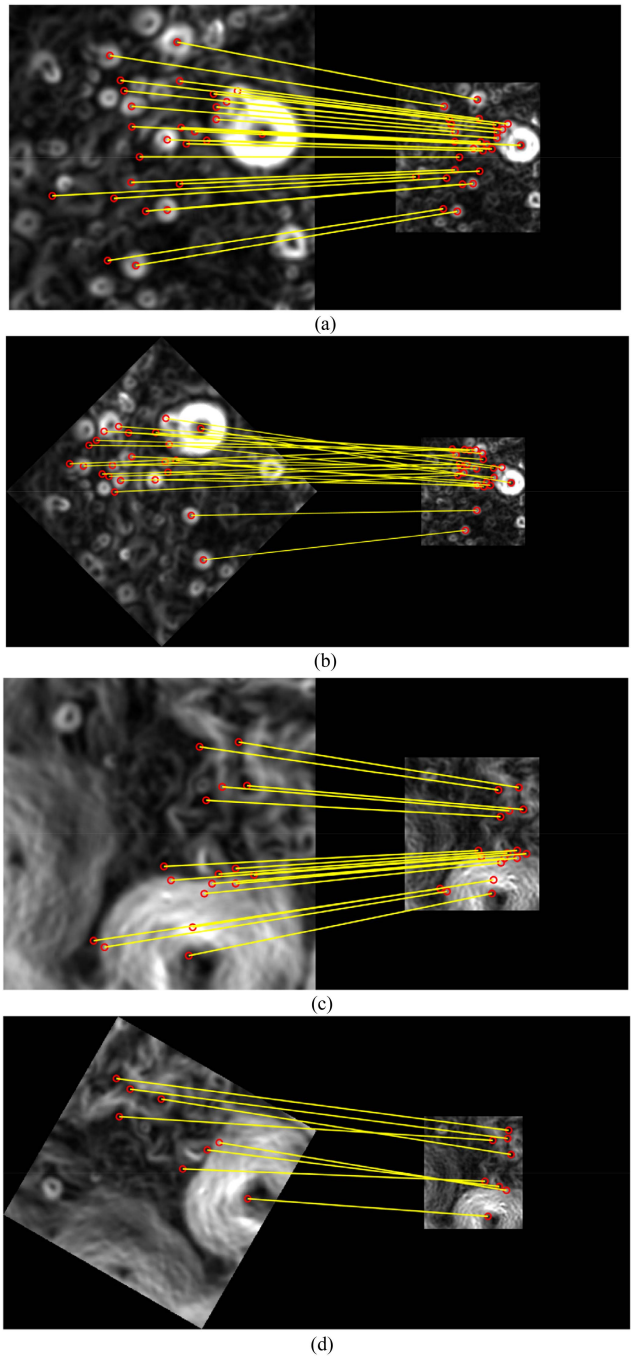

Fig. 7. Right image is the reference image from InSAR with spatial resolution of 20 m/pixel. The left image is the real-time image with spatial resolution of 10 m/pixel. The matched images of PSR in crater shoemaker: (a) rotation angle of the real-time image is 0°; and (b) rotation angle of the real-time image is 45°. The matched images of PSR in crater Shackleton: (c) rotation angle of the real-time image is 0°; and (d) rotation angle of the real-time image is 60°.

over the floor BC in SAR image, as shown in Fig. 8. It is difficult to calculate the interference phase of these regions.

For craters whose diameters are in the range of 5–120 km, the slope angles of the crater wall are in the range of nearly 0° to 31.5° [31]. Fig. 9 shows the probability density function of the slope angles of the lunar south pole [7]. In total, 99.9% slope angles are smaller than 35°, and 99.4% slope angles are smaller

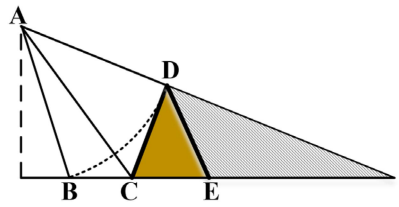

Fig. 8. Shadow and layover in SAR image.

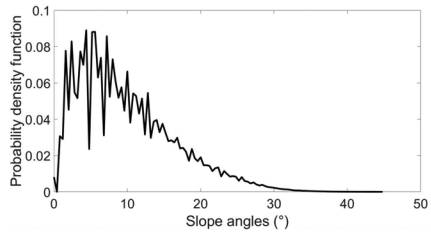

Fig. 9. Probability density function of slope angles at the lunar south pole.

than 30°. The slope angle of the crater Shackleton at south pole can reach 35°.

To detect these craters with SAR, layover and shadow effects need to be avoided. Given that the slope angle of the crater wall is γ, the incidence angle should satisfy

$$\gamma < \theta_i < 90 - \gamma. \tag{20}$$

To avoid layover when mapping the topography of lunar surface pole, an incidence angle that is larger than 35° is suggested.

VI. Conclusion

In this article, the DEM data are generated with the simulated InSAR images. With the SURF algorithm, the DEM generated with InSAR technology can be used for TRN in PSR on the Moon. The radar echoes from the PSRs in crater Shoemaker and Shackleton at lunar south pole are simulated with DEM data and two-scale rough surface model. The RDA is utilized to produces the lunar SAR image. With the interference phases between the simulated SAR images from two antennas, the DEM data of PSR are generated. The slope angles are calculated with the generated DEM data after geometric correction. For TRN, the slope angle images from InSAR observations are taken as reference images. The high-resolution DEM data from LOLA are taken as the real-time image from the flyer. With the SURF algorithm, the reference images are matched with real-time images to determine the real-time position and motion vector of the flyer. The results prove that InSAR technology and the SURF algorithm will be helpful in determining the position and motion vector of the flyer in PSR.

Acknowledgment

The authors would like to thank the LOLA operations teams for the collection of the high-quality datasets used in this work. The data used in this study are publicly available via the Geosciences Node of the Planetary Data System (http://pds-geosciences.wustl.edu).

REFERENCES

[1] D. A. Paige et al., "Diviner lunar radiometer observation of cold traps in the Moon's South polar region," *Science*, vol. 330, no. 6003, pp. 479–482, 2010.

[2] Y. Zou, Y. Liu, and Y. Jia, "Overview of China's upcoming Chang'E series and the scientific objectives and payloads for Chang'E-7 mission," in *Proc. 51st Annu. Lunar Planet. Sci. Conf.*, 2020, Art. no. 1755.

[3] M. K. Barker et al.," Improved LOLA elevation maps for south pole landing sites: Error estimates and their impact on illumination conditions," *Planet. Space Sci.*, vol. 203, 2021, Art. no. 105119, doi: 10.1016/j.pss.2020.105119.

[4] G. Wei et al., "Illumination conditions near the Moon's south pole: Implication for a concept design of China's Chang'E−7 lunar polar exploration," *Acta Astronautica*, vol. 208, pp. 74–81, 2023.

[5] N. Liu and Y.-Q. Jin, "Selection of a landing site in the permanently shadowed portion of lunar polar regions using DEM and Mini-RF data," *IEEE Geosci. Remote Sens. Lett.*, vol. 19, Dec. 2022, Art. no. 4503305, doi: 10.1109/LGRS.2021.3138071.

[6] N. Liu and Y.-Q. Jin, "Terrain relative navigation at the lunar poles with DEM data and SURF algorithm," *IEEE Geosci. Remote Sens. Lett.*, early access, 2023.

[7] D. E. Smith et al., "Summary of the results from the lunar orbiter laser altimeter after seven years in lunar orbit," *Icarus*, vol. 283, pp. 70–91, 2017.

[8] S. Li, X. Jiang, and T. Tao, "Guidance summary and assessment of the Chang'E-3 powered descent and landing," *J. Spacecraft Rockets*, vol. 53, no. 2, pp. 1–20, 2016.

[9] R. K. Raney et al., "The lunar Mini-RF radars: Hybrid polarimetric architecture and initial results," *Proc. IEEE*, vol. 99, no. 5, pp. 808–823, May 2011.

[10] S. S. Bhiravarasu et al., "Chandrayaan-2 dual-frequency synthetic aperture radar (DFSAR): Performance characterization and initial results," *Planet. Sci. J.*, vol. 2, no. 134, 2021, doi: 10.3847/PSJ/abfdbf.

[11] Y. Gao et al., "Analysis of rock abundance on lunar surface and near-surface using Mini-RF SAR data," *IEEE J. Sel. Topics Appl. Earth Observ. Remote Sens.*, vol. 16, pp. 9590–9605, Oct. 2023, doi: 10.1109/JSTARS.2023.3323510.

[12] Y. Gao et al., "Investigating the dielectric properties of lunar surface regolith fines using Mini-RF SAR data," *Int. Soc. Photogrammetry Remote Sens. J. Photogrammetry Remote Sens.*, vol. 197, pp. 56–70, Mar. 2023.

[13] Y. Wang et al., "Lunar microwave imaging radar (LMIR)," in *Proc. 14th Eur. Conf. Synthetic Aperture Radar*, 2022, pp. 1–3.

[14] D. G. Lowe, "Distinctive image features from scale-invariant keypoints," *Int. J. Comput. Vis.*, vol. 60, pp. 91–110, 2004.

[15] H. Bay et al., "Speeded-up robust features (SURF)," *Comput. Vis. Image Understanding*, vol. 110, no. 3, pp. 346–359, 2008.

[16] N. Liu and Y. Q. Jin, "Simulation of Pol-SAR imaging and data analysis of Mini-RF observation from the lunar surface," *IEEE Trans. Geosci. Remote Sens.*, vol. 60, Mar. 2022, Art. no. 2000411, doi: 10.1109/TGRS.2021.3064091.

[17] F. T. Ulaby and D. G. Long, *Microwave Radar and Radiometric Remote Sensing*. Ann Arbor, MI, USA: Univ. of Michigan Press, 2015, pp. 163–172.

[18] N. Liu and Y. Q. Jin, "Pol-SAR image simulation of the lunar surface with data analysis of Chandrayaan-2 and Mini-RF," *IEEE J. Sel. Topics Appl. Earth Observ. Remote Sens.*, vol. 16, pp. 10301–10310, Oct. 2023, doi: 10.1109/JSTARS.2023.3328063.

[19] G. D. Martino, A. Iodice, D. Poreh, and D. Riccio, "Pol-SARAS: A fully polarimetric SAR raw signal simulator for extended soil surfaces," *IEEE Trans. Geosci. Remote Sens.*, vol. 56, no. 4, pp. 2233–2247, Apr. 2018.

[20] Y. Q. Jin, *Electromagnetic Scattering Modelling for Quantitative Remote Sensing*. Singapore: World Scientific, 1993, pp. 288–317.

[21] F. T. Ulaby, R. K. Moore, and A. K Fung. *Radar Remote Sensing and Surface Scattering and Emission Theory. Microwave Remote Sensing Active & Passive II*, Norwood, MA, USA: Artech House, 1982, pp. 922–962.

[22] G. H. Heiken et al., *Lunar Sourcebook: A User's Guide to the Moon*. Cambridge, U.K.: Cambridge Univ. Press, 1991, pp. 536–584.

[23] M. Shimada, *Imaging From Spaceborne and Airborne SARs, Calibration, and Applications*, Boca Raton, FL, USA: CRC Press, 2019, pp. 17–66.

[24] I. G. Cumming and F. H. Wong, *Digital Processing of Synthetic Aperture Radar Data: Algorithms and Implementation*. Beijing, China: Publishing House of Electron. Ind., 2007, pp. 179–191.

[25] R. Bamler and P. Hartl, "Synthetic aperture radar interferometry," *Inverse Problems*, vol. 14, p. R1, 1998, doi: 10.1088/0266-5611/14/4/001.

[26] P. A. Rosen et al., "Synthetic aperture radar interferometry," *Proc. IEEE*, vol. 88, no. 3, pp. 333–382, Mar. 2000.

[27] H. A. Zebker, C. L. Werner, P. A. Rosen, and S. Hensley, "Accuracy of topographic maps derived from ERS-1 interferometric radar," *IEEE Trans. Geosci. Remote Sens.*, vol. 32, no. 4, pp. 823–836, Jul. 1994.

[28] S. Li et al., "Direct evidence of surface exposed water ice in the lunar polar regions," *Proc. Nat. Acad. Sci. USA*, vol. 115, no. 36, pp. 8907–8912, 2018.

[29] B. A. Campbell, "*Radar Remote Sensing of Planetary Surfaces*," Cambridge, U.K.: Cambridge Univ. Press, 2002, pp. 110–117.

[30] P. H. S. Torr and A. Zisserman, "MLESAC: A new robust estimator with application to estimating image geometry," *Comput. Vis. Image Understanding*, vol. 78, no. 1, pp. 138–156, 2000.

[31] C. K. Sim et al., "Asymmetric space weathering on lunar crater walls," *Geophysical Res. Lett.*, vol. 44, no. 22, pp. 11273–11281, 2017.

Niutao Liu (Member, IEEE) was born in Jiangsu, China, in 1994. He received the B.S. degree in telecommunication engineering from the Nangjing University of Posts and Telecommunications, Nanjing, China, in 2016, and the Ph.D. degree in electromagnetic field and microwave technology from Fudan University, Shanghai, China, in 2021.

He is currently an Assistant Professor with the Key Laboratory for Information Science of Electromagnetic Waves (MoE), Fudan University. His research interests include microwave planetary remote sensing, infrared remote sensing, computational electromagnetics, and synthetic aperture radar data analysis.

Ya-Qiu Jin (Life Fellow, IEEE) received the B.S. degree in atmospheric physics from Peking University, Beijing, China, 1970, and the M.S., E.E., and Ph.D. degrees in electrical engineering and computer science from the Massachusetts Institute of Technology, Cambridge, MA, USA in 1982, 1983, and 1985, respectively.

He was the Research Scientist with Atmospheric Environmental Research, Inc., Cambridge, in 1985, a Research Associate Fellow with the City University of New York, in 1986–1987, and a Visiting Professor with the University of York, U.K., in 1993, sponsored by the U.K. Royal Society. He is currently the Te-Pin Professor, and the Director with the Key laboratory for Information Science of Electromagnetic Waves (MoE), and Institute of EM Big data and Intelligence Remote Sensing, Fudan University, Shanghai, China. He has authored and co-authored more than 850 papers in refereed journals and conference proceedings and 17 books, including *Polarimetric Scattering and SAR Information Retrieval* (Wiley and IEEE, 2013), *Theory and Approach of Information Retrievals From Electromagnetic Scattering and Remote Sensing* (Springer, 2005), and *Electromagnetic Scattering Modelling for Quantitative Remote Sensing* (World Scientific, 1994). His main research interests include electromagnetic scattering and radiative transfer in complex natural media, microwave satellite-borne remote sensing, as well as theoretical modeling, information retrieval and applications in earth terrain and planetary surfaces, and computational electromagnetics.

Dr. Jin was the recipient of the Senior Research Associateship in NOAA/NESDIS by USA National Research Council in 1996. He is the Academician of the Chinese Academy of Sciences, and a Fellow of the World Academy of Sciences for Advances of Developing World and International Academy of Astronautics. He was one of the first group of the IEEE Geoscience and Remote Sensing Society (GRSS) Distinguished Speakers. He was the Co-Chair of the Technical Program Committee for IEEE International Geoscience and Remote Sensing Symposium (IGARSS) 2011, Vancouver, Canada, and Co-General Chair for IGARSS2016, Beijing, China. He was the Associate Editor for IEEE TRANSACTIONS ON GEOSCIENCE AND REMOTE SENSING (2005–2012) and IEEE ACCESS (2016–2018); the Member of IEEE GRSS AdCom; and the Chair for IEEE Fellow Evaluation of GRSS (2009–2011). He is currently the Member of IEEE GRSS Major Awards Committee. He was the recipient of the first-grade MoE Science Prizes in 1992, 1996, and 2009; IEEE GRSS Education Award in 2010; the China National Science Prize in 1993 and 2011; the IEEE GRSS Distinguished Achievement Award in 2015; the Shanghai Sci/Tech Gong-Cheng Award in 2015; and the Golden Florin Award in 2022, among many other prizes.